PROCEEDINGS, 43rd Workshop on Geothermal Reservoir Engineering
Stanford University, Stanford, California, February 12-14, 2018
SGP-TR-213

$\underline{\alpha\varphi} \sim \underline{\alpha\varphi}_{crit} \sim$ Basement Rock EGS as Extension of Reservoir Rock Flow Processes

Peter Leary[1], Peter Malin[1], Tero Saarno[2] and Ilmo Kukkonen[3]
1 Advanced Seismic Instrument & Research, 1311 Waterside, Dallas, TX 75218-4475, USA;
pcl@asirseismic.com pem@asirseismic.com
2 St1 Deep Heat Oy, Purotie 1/PL 100, 00381 Helsinki, Finland;
tero.saarno@st1.fi
3 Department of Physics, University of Helsinki, P.O. Box 64, 00014 Helsinki, Finland;
ilmo.kukkonen@helsinki.fi

Keywords: Porosity, permeability, fractures, fracture connectivity, spatial correlation, criticality, Ising model

ABSTRACT

Crustal reservoir well-core sequences measured for porosity φ and permeability κ show a clear linear trend, $\log\kappa \sim \alpha\varphi$, when plotted as an ordered sequence in porosity. For porosity expressed as a fraction of rock volume, $0 < \varphi < 1$, the observed proportionality constant α is of order $15 < \alpha < 35$ for standard reservoir rock in porosity range $0.1 < \varphi < 0.3$, and of order $300 < \alpha < 700$ for crystalline rock in porosity range $0.001 < \varphi < 0.01$. When porosity φ decreases an order of magnitude in basement crystalline rock, the proportionality parameter α increases an order of magnitude. The parameter value $\underline{\alpha\varphi} \sim 3\text{-}4$ is thus observed over more than two orders of magnitude porosity range, $\sim 0.001\text{-}.01 < \varphi < \sim 0.1\text{-}0.3$. Parallel evidence consistent with parameter values $\underline{\alpha\varphi} \sim 3\text{-}4$ emerges upon integrating well-core data sequences sampled at dm-to-m increments to give relation $\kappa \sim \kappa_0 \exp(\alpha\varphi)$ for well-productivity in the Dm-to-Hm scale range. Wellbore productivity is observed to be lognormally distributed for flow of basement rock groundwater, conventional/unconventional hydrocarbons, convective geothermal fluids, and fossil fluid systems that generate mineral deposits. The probability density function $\exp(\alpha\varphi)$ gives lognormal distributions for $\underline{\alpha\varphi} \sim 3\text{-}4$. The empiric $\underline{\alpha\varphi} \sim 3\text{-}4$ is also consistent with well-log spatial fluctuation power-spectral amplitudes throughout the crust. Power-law scaling $S(k) \propto 1/k$, $\sim 1/\text{km} < k < \sim 1/\text{cm}$, applies equally to well-log fluctuations in imporous/impermeable crystalline/metamorphic/basement rock and in porous/permeable reservoir rock. Power-law scaling spatial fluctuations in geological media imply a critical state crustal process which generates the long-range spatial correlations attested in well-log spectral scaling, and the long-range grain-scale spatial-connectivity fluid flow structures observed in well production lognormality. With EGS stimulation via wellbore-centric fluid pressurization in mind, we adduce further evidence for $\underline{\alpha\varphi} \sim 3\text{-}4$ by quantifying the effect on inter-granular fluid flow of introducing a single grain-scale pore into an existing poroperm structure with n pores, $n \rightarrow n+1$. The effect of incremental increase in porosity on fluid flow velocity in a crustal volume is greater for granular percolation flow than for the smooth Poiseuille flow typically assumed for standard fracture-flow models. Expending EGS crustal deformation energy on creating flow-related defects is two to three times more effective in accommodating fluid pressure for granular percolation flow than for creating open fractures as in past EGS stimulation models. We can thus expect EGS wellbore fluid pressurisation to preferentially increase crustal fluid flow capacity through incrementing porosity associated with granular percolation flow structures than through creating smooth-fracture flow-conduits. As attempts at EGS basement rock stimulation via generating planar fracture surfaces have repeatedly failed, our $\underline{\alpha\varphi} \sim 3\text{-}4$ inference accords well with field-scale stimulation experience. The underlying physics implied by crustal flow empirics can be readily expressed by adapting the 2d/3d Ising model of critical-state ferromagnetism to fluid flow in granular media, with $\underline{\alpha\varphi} \sim \underline{\alpha\varphi}_{crit} \sim 3\text{-}4$ playing a decisive role as critical-state system parameter. Accordingly, it would seem likely that the observed rock-fluid interaction empirics are fundamental physical statements about the crustal brittle-fracture domain, and as such should be incorporated into EGS projects.

1. INTRODUCTION

A large volume of well-log, well-core, and well-flow empirical evidence defines the pervasive spatial-correlation nature of fluid flow through crustal reservoir rock. Well-log spatial fluctuations in geological settings worldwide are characterised by power-law spectral scaling in spatial frequency k, $S(k) \propto 1/k^1$, over five to six orders of scale magnitude, $\sim 1/\text{cm} < k < \sim 1/\text{km}$ [1]. Well-core sequences from hydrocarbon-bearing crustal reservoir formations worldwide show that spatial variations in porosity correlate with spatial variations in the logarithm of permeability, $\delta\varphi \propto \delta\log\kappa$, over m-Hm scale lengths [2-3]. Crustal permeability κ at the scales of well-flow productivity is lognormally distributed for groundwater, conventional and unconventional hydrocarbons, and geothermal fluids, along with the mineral deposits of fossil flow systems, as given by $\kappa \propto \exp(\alpha\varphi)$ for normally distributed porosity φ in association with observed values of empirical poroperm parameter α [3-4].

At least two questions arise from these crustal fluid flow spatial-correlation empirics:

- How do fluid-rock interactions generate the spatially-correlated lognormal fluid flow distributions abundantly seen in crustal reservoir formations for porosity range $0.1 < \varphi < 0.3$?
- What happens to crustal fluid flow properties when porosity decreases by an order of magnitude, $\varphi < 0.01$, at increasing crustal depths?

The answers to these two questions appear to be closely linked. Data on fluid flow in tight crystalline rock indicate that the long-range spatial-correlation empirics of crustal reservoir flow persist to porosities $\varphi < 0.01$ and permeabilities $\kappa < \mu D$ characteristic of rock at the

5-10 km depth range. More specifically, a fixed mean product magnitude $\underline{\alpha\varphi}$ ~ 3-4 characteristic for a range of hydrocarbon-bearing sandstones is observed to persist in low-poroperm crystalline basement rock. An order-of-magnitude decrease in basement rock porosity, $\varphi < 0.01$, compensated by empirical parameter α increasing by an order of magnitude, α ~ 300-400, gives parameter product estimates of $\underline{\alpha\varphi}$ ~ 1.5-3.5. An essentially fixed magnitude for poroperm parameter $\underline{\alpha\varphi}$ over a 2-decade crustal rock porosity range $0.003 < \varphi < 0.3$ implies that crustal rock spatial correlations $S(k) \propto 1/k$ and lognormal well-flow distributions $\kappa \propto \exp(\alpha\varphi)$ over a wide range of crustal fluids and geological settings are associated with $\underline{\alpha\varphi}$ ~ 3-4 as fundamental to the physics of crustal rock-fluid interactions.

The empirics of crustal rock power-law-scaling spatial correlation in company with a fixed system parameter, here $\underline{\alpha\varphi}$ ~ 3-4 associated with lognormal permeability distributions, have clear parallels in physical systems undergoing a class of thermodynamic phase transition. Examples of such phase transition macroscale collective behaviour of microscale system elements at a fixed system temperature are ferromagnetism in iron atom assemblages and density fluctuations in liquid-gas interface states [5]. The observed physical system macroscale spatial correlation properties are in turn closely replicated by numerical simulations with the Ising model mathematical representation of ferromagnetic and liquid-gas spatial fluctuation states [5-8]. An Ising model numerical representation of crustal rock-fluid interactions between active grain-scale crustal elements provides a compelling perspective on the long-range spatial correlation empirics of crustal flow systems.

A physics-based interpretation of crustal fluid flow heterogeneity generated by spatially-correlated interaction of system elements at all scale lengths is a vast improvement over the statistics-friendly default assumption that rock-fluid interactions are effectively spatially uncorrelated at essentially all scales and hence their spatial fluctuations can be simply ignored by averaging over relevant spatial domains [9-16]. The assumed quasi-uniformity that spatial averaging gives to the mechanical properties of crustal rock has typically been the basis for projects to engineer or enhance increased crustal permeability for heat energy extraction [17-20]. These crustal flow stimulation attempts have not met with success [21-24].

Application of the Ising model to crustal fluid flow empirics can bring conceptual clarity to an economically important topic that remains poorly understood in physical terms and poorly handled by application of standard statistical assumptions. After illustrating how the Ising model reproduces spatial correlation empirics of crustal rock for an assumed critical-state parameter, we support the Ising model application to crustal rock-fluid interaction empirics with evidence for the parameter value $\underline{\alpha\varphi}$ ~ 3-4. Some three thousand well-core samples from hydrocarbon reservoir rock provide the estimate $\underline{\alpha\varphi} \sim 3.74 \pm 0.91$. We then review crystalline rock well-core and well-flow evidence that a decade drop in porosity, $\varphi < 0.01$, is accompanied by decade rise in α ~ 300-700 to maintain the parameter value $\underline{\alpha\varphi}$ ~ 1.5-3.5. A discussion section detailing the analogy between the Ising model and crustal rock-fluid interaction leads to a concluding section aimed at defining the engineering mechanics needed for wellbore-to-wellbore flow stimulation in low-porosity/low-permeability basement rock. Achieving adequate wellbore-to-wellbore flow in the deep crust gives access to the 10^8 quads of carbon-free heat energy that exceed by a factor 100 the $0.5 \cdot 10^6$ quads held in the earth's fossil fuel store.

2. THE ISING MODEL

The Ising model mathematically simulates the collective spatial-correlation interactions of ferromagnetic atoms and liquid-gas system molecules that occur during system critical-state phase transitions [5-6]. The model is based on a lattice system of energy-interaction nodes in either 2 or 3 dimensions. Each Ising model lattice node is the site of an active system element ('atom' or 'molecule') that can be in one of two interaction-energy states. For ferromagnetism, the nodal interaction-energy states are associated with the alignment or anti-alignment of the iron atom magnetic dipole with an applied magnetic field. For the liquid-gas phase transition, the nodal interaction-energy states are associated with the low or high compressibility of a unit of liquid-gas volume. To represent collective behaviour in a crustal rock-fluid system, we identify the Ising model interaction-energy nodal states with grain-scale fluid flow conditions: a nodal state that permits grain-scale fluid flow between nearby pores, and a nodal state that blocks grain-scale fluid flow between nearby pores.

In making this nodal interaction-energy assignment for crustal rock-fluid interaction, we are in effect asking if the interaction-energy state of one grain-scale flow condition can significantly influence the interaction energy state of nearby grain-scale flow conditions? And if such grain-scale flow/no-flow energy-interactions occur, can these interactions lead to long-range macroscopic collective spatial organisation in which spatial groupings of grain-scale flow conditions influence other groupings of grain-scale flow conditions in the scale-independent manner observed in ferromagnetic and liquid-gas phase transitions?

The great power of the Ising model is that a 2d model lattice of interacting nodal energy states mathematically guarantees the existence of a system energy state that reproduces the spatially-correlated collective action we seek to replicate [6]. In the context of the second law of thermodynamics, if the Ising lattice nodal interaction-energy is large enough relative to the mean thermal energy at each node, then it is mathematically certain for a 2d lattice that at a specific mean nodal thermal energy, node-node interaction-energy states will behave collectively to replicate the physical behaviour of ferromagnetic and liquid-gas phase transitions, and by extension the empirics of the crustal rock-fluid flow.

Figure 1 illustrates how Ising model microscale interaction-energy states interact to replicate the spatial complexity empirics of crustal fluid-rock interactions. In applying the Ising model, it is assumed that the empirical rock-fluid interaction parameter $\underline{\alpha\varphi}$ duplicates the role of mean system equilibrium temperature $\underline{\theta}$ in controlling the spatial-correlation properties of crustal rock-fluid interaction heterogeneity. The Figure 1 model spatial correlations are produced by Matlab code given in the Appendix 1.

The control parameter in Figure 1 Ising model spatial-correlation phenomenology is the lattice system thermal equilibrium mean energy $\underline{\theta}$ relative to the mathematically-guaranteed critical-state temperature $\underline{\theta}_{crit}$. The left-hand nodal-energy spatial distribution is for $\underline{\theta} = \underline{\theta}_{high}$

$> \underline{\theta}_{crit}$. At this system energy, Ising lattice nodal interaction energies are uncorrelated at all scale lengths; the spatial fluctuations recorded by a transecting well-log correspond to white noise with flat power-spectral scaling $S(k) \propto 1/k^0$. The right-hand nodal-energy distribution is for $\underline{\theta} = \underline{\theta}_{low} < \underline{\theta}_{crit}$. At this system energy, Ising lattice nodes approach maximum spatial correlation at all scale lengths, with well-log spatial fluctuation spectra corresponding to strong partition of nodal energy states as given by the power-spectrum of a step-function, $S(k) \propto 1/k^2$. The center nodal-energy distribution is for $\underline{\theta} \sim \underline{\theta}_{crit}$, the mathematically guaranteed Ising model system energy at which long-range spatially-correlated phase transitions occur. For $\underline{\theta} \sim \underline{\theta}_{crit}$, the corresponding lattice nodal energy fluctuations recorded by well-logs through the medium replicates the crustal rock-fluid interaction spatial-correlation power-spectral condition $S(k) \propto 1/k^1$ seen in well-log spatial fluctuation power-spectral scaling worldwide [1].

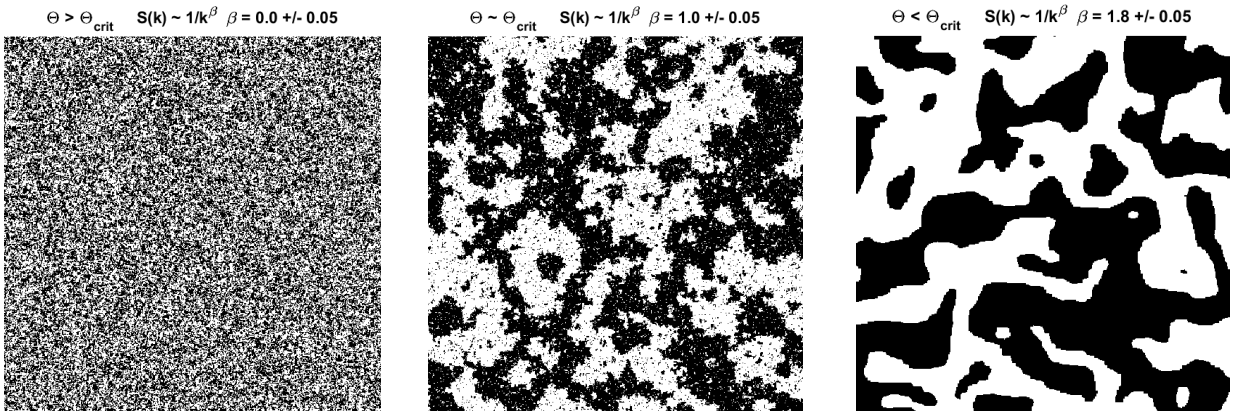

Figure 1 -- Ising 2d model spatial distributions of lattice nodal interaction-energy for three values of system equilibrium thermal energy $\underline{\theta}$ relative to a critical state thermal energy $\underline{\theta}_{crit}$ that is mathematically known to exist. (Left) System thermal energy $\underline{\theta} > \underline{\theta}_{crit}$, in which nodal thermal energy is too high for node-node interactions; the resulting nodal energy distribution is white noise with zero spatial correlation generating well-log spectral scaling $S(k) \propto 1/k^0$ over 3 decades of scale length. (Right) System thermal energy $\underline{\theta} < \underline{\theta}_{crit}$, in which nodal thermal energy is dominated by node-node interaction energy; the resulting nodal energy distribution is red noise with high degree of spatial correlation, with well-log spectral scaling $S(k) \propto 1/k^{1.8}$ over 3 decades of scale length. (Center) System thermal energy $\underline{\theta} \sim \underline{\theta}_{crit}$, with nodal thermal energy comparable to node-node interaction energy; the resulting nodal energy distribution is pink noise with moderate degree of spatial correlation, giving well-log spectral scaling $S(k) \propto 1/k^1$ over 3 decades of scale length. The Ising model application to crustal rock-fluid interactions implies that the empirical crustal parameter $\underline{\alpha\varphi} \sim$ 3-4 plays the role of the mathematically mandated critical mean thermal energy $\underline{\theta}_{crit}$.

Interpreting Figure 1 Ising model spatial distributions of lattice nodal energies in terms of crustal rock-fluid interactions, the $S(k) \propto 1/k^1$ transition spatial correlation state of crustal rock-fluid interaction empirics lies between a high energy crustal rock state, $\underline{\theta} > \underline{\theta}_{crit}$, that corresponds to chemical and mechanical disaggregation of cements and mineral grains at uppermost crustal depths, and a low energy crustal rock state, $\underline{\theta} < \underline{\theta}_{crit}$, that corresponds to chemical and mechanical homogenization of cements and mineral grains by ductile deformation at lower crustal depths. Prospectively, the crustal rock-fluid interaction poroperm parameter values $\underline{\alpha\varphi} \sim$ 3-4, which occur across two-decades crustal porosity $0.003 < \varphi < 0.3$ in association with $S(k) \propto 1/k^1$ spatial correlations, correspond to the Ising model critical energy $\underline{\theta}_{crit}$. The existence of a fixed crustal rock-fluid interaction poroperm parameter $\underline{\alpha\varphi} \sim$ 3-4 is logically equivalent to Ising model system equilibrium thermal energy $(\underline{\alpha\varphi})_{crit} \equiv \underline{\theta}_{crit}$. Values of $\underline{\alpha\varphi}$ significantly above and below the critical state value $(\underline{\alpha\varphi})_{crit}$ characterise the very different uppermost- and lower-crustal rock-fluid interaction regimes. From the Figure 1 spatial-correlation systematics, it follows that vanishing crustal porosity levels, $\underline{\alpha\varphi} < (\underline{\alpha\varphi})_{crit}$, correspond to the ductile deformation state of rock in the lower crust ($S(k) \propto 1/k^2$), and excessive crustal porosity levels correspond to the disaggregation state of uppermost crustal rock ($S(k) \propto 1/k^0$).

3. EVIDENCE FOR $\underline{\alpha\varphi} \sim$ 3-4 IN HYDROCARBON RESERVOIR FORMATIONS

Well-core from exploratory wells in conventional hydrocarbon reservoirs are typically available to estimate the total hydrocarbon reserve (formation porosity) and its production rate (formation permeability). As such, there are many poroperm data at intervals of order 1 meter over Dm- to Hm-scale formations with porosity of order $0.1 < \varphi < 0.3$ and permeabilities of order $0.01\text{mD} < \kappa < 100\text{mD}$ (10^{-17}–10^{-13}m^2).

Well-core sequences from hydrocarbon-bearing reservoir formations worldwide show variation in porosity to be spatially correlated with variation in the logarithm of permeability, $\delta\varphi \propto \delta\log\kappa$ [2-4]. The proportionality constant α for this spatial correlation relation is estimated by plotting $\log\kappa$ against φ for suites of well-core poroperm data from hydrocarbon reservoir formations.

The five following tables and figures estimate the proportionality parameter α for representative hydrocarbon-bearing sandstone formations: (i) Tirrawarra gas field, South Australia; (ii) Toolachee gas field, South Australia; (iii) Brae oil field, North Sea; (iv) Bierwang gas field, Germany; (v) Lewis Shale, Wyoming. For each poroperm sample, the relation $\delta\varphi \sim \alpha\ \delta\log\kappa$ is pictured, with a table supplying the formation or well name, number of core samples giving both porosity and permeability over a limited depth range (Dm for gas field, Hm for oil field), core sample depth interval, minimum, maximum, and median well-core porosity percentages,

minimum and maximum permeability in milliDarcies, percentage spatial-correlation of the porosity versus logarithm of permeability poroperm spatial fluctuation sequence, value of α, and value of the product parameter $\underline{\alpha\varphi}$.

Table 1 collects the $\underline{\alpha\varphi}$ mean value estimates for the five hydrocarbon reservoir sites. For comparison, also given are $\underline{\alpha\varphi}$ well-core determinations from the KTB deep well in Germany and well-core + well-flow data from the Borrowdale Volcanics crystalline rock near Sellafield nuclear facility, Cumbria, UK presented below.

Table 1 – Mean $\underline{\alpha\varphi}$ poroperm properties for five hydrocarbon-bearing formations and two crystalline rock formations

SITE	Sample #	Sample Mean $\underline{\alpha\varphi}$
Tirrawarra gas field, South Australia	691	$\underline{\alpha\varphi} = 3.82 \pm 0.95$
Toolachee gas field, South Australia	251	$\underline{\alpha\varphi} = 4.06 \pm 1.00$
Brae oil field, North Sea	757	$\underline{\alpha\varphi} = 2.71 \pm 0.38$
Bierwang gas field, Germany	1189	$\underline{\alpha\varphi} = 3.90 \pm 0.72$
Lewis Shale analogue reservoir, Wyoming	131	$\underline{\alpha\varphi} = 4.22 \pm 1.5$
KTB, Germany (4-6 km)	31	$\underline{\alpha\varphi} = 1.3 \pm 0.05$
Borrowdale Volcanics, Sellafield, Cumbria, UK	--	$\underline{\alpha\varphi} = 4.6 \pm 1.2$

2.1 Tirrawarra gas field, South Australia

Table 2 – Well-core φ-log(κ) data for Tirrawarra gas field formations.

FORMATION	Sample #	Z_{mn} (m)	Z_{mx} (m)	φ_{mn} (%)	φ_{mx} (%)	φ_{md} (%)	κ_{mn} (mD)	κ_{mx} (mD)	χ(%)	α	$\underline{\alpha\varphi}$
TIRRAWARRA A	63	2694	2786	2	16	11	0.0770	126	55	22	2.42
TIRRAWARRA B	73	2838	2885	5	15	10	0.0400	46	57	22	2.20
TOOLACHEE A	53	1949	1997	8	23	16	0.0100	551	56	31	4.96
TOOLACHEE B	41	2087	2103	2	20	9	0.0100	393	84	29	2.61
HUTTON	20	1817	1850	4	21	12	0.0070	2140	69	33	3.96
NAMUR A	29	1235	1256	6	29	25	0.0400	2281	57	18	4.50
NAMUR C	32	1517	1549	4	23	20	0.0230	2799	67	24	4.80
NAMUR D	34	1578	1587	8	24	20	0.2000	1560	52	20	4.00
NAMUR E	42	1752	1768	10	18	15	0.3750	1213	49	31	4.65
BIRKHEAD A	25	1559	1574	7	25	22	0.0050	1649	62	21	4.62
BIRKHEAD B	47	1639	1657	12	27	22	0.7120	4880	41	18	3.96
BIRKHEAD C	110	1814	1842	3	22	11	0.0010	2018	44	27	2.97
MCKINLAY	122	1176	1256	7	28	20	0.0050	2869	52	20	4.00

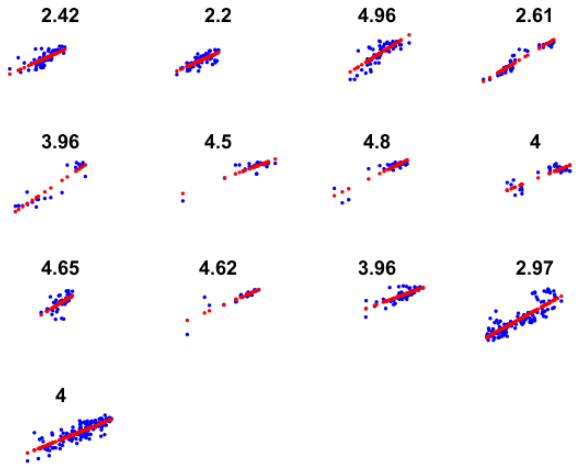

Figure 2 – Well-core φ-log(κ) linear relation for Tirrawarra gas field formations (Table 1); each subplot is titled with value $\underline{\alpha\varphi}$ given by linear trend coefficient α and mean porosity $\underline{\varphi}$.

2.2 Toolachee gas field, South Australia

Table 3 – Well-core φ-log(κ) data for Toolachee gas field formations.

FORMATION	Sample #	Z_{mn} (m)	Z_{mx} (m)	φ_{mn} (%)	φ_{mx} (%)	φ_{md} (%)	κ_{mn} (mD)	κ_{mx} (mD)	χ(%)	α	$\underline{\alpha\varphi}$
MURTA	33	1192	1244	12	23	19	0.64	2550	77	28.2	5.35
MURTA	96	1202	1253	9	28	20	0.51	1717	89	22.7	4.54
DARALINGIE	31	2387	2793	4	19	14	0.60	576	82	24.2	3.39
TOOLACHEE	18	2381	2573	9	14	11	0.53	213	95	47.7	5.25
PATCHAWARRA	43	2243	2284	9	20	15	1.50	439	84	25.8	3.88
BIRKHEAD	16	1616	1635	10	25	20	0.82	792	72	15.2	3.04
PATCHAWARRA	14	2913	2935	8	15	9	0.51	137	96	33.2	2.99

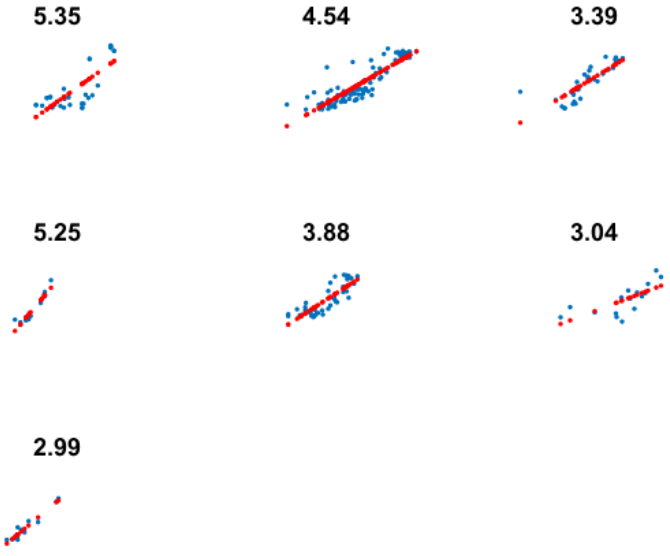

Figure 3 – Well-core φ-log(κ) linear relation for Toolachee gas field formations (Table 2); each subplot is titled with value $\underline{\alpha\varphi}$ given by linear trend coefficient α and mean porosity $\underline{\varphi}$.

2.3 Brae oil field, North Sea

Table 4 – Well-core φ-log(κ) data for Brae oil field formations

WELL #	Sample #	Z_{mn} (m)	Z_{mx} (m)	φ_{mn} (%)	φ_{mx} (%)	φ_{md} (%)	κ_{mn} (mD)	κ_{mx} (mD)	χ(%)	α	$\underline{\alpha\varphi}$
BRAE_16_7_3	141	8	809	1.6	15	10	0.0060	74	83	25.3	2.53
BRAE_16_7A_27	46	56	384	2	17	11	0.2200	502	83	25.7	2.93
BRAE_16_7A_22	261	970	1426	1.5	22	12	0.0200	1990	79	25.9	3.11
BRAE_16_7A_C5	118	179	456	1.7	18	11	0.0400	669	74	20.2	2.17
BRAE_16_7A_C5a	86	458	732	2.0	18	12	0.0500	625	75	21.1	2.45
BRAE_16_7A_C3	105	581	1470	1.4	24	120	0.1000	2960	86	25.8	3.09

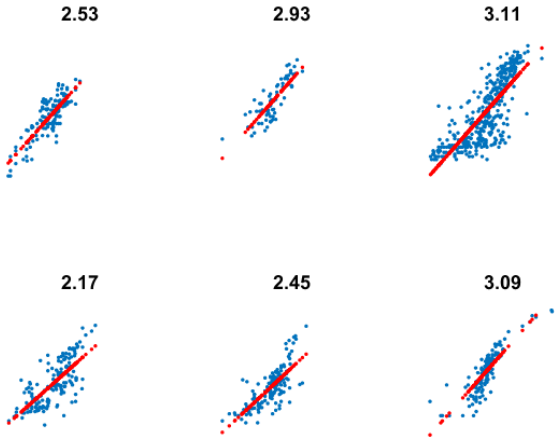

Figure 4 – Well-core φ-log(κ) linear relation for Brae oil field formations (Table 3); each subplot is titled with value $\underline{\alpha\varphi}$ given by linear trend coefficient α and mean porosity $\underline{\varphi}$.

2.4 Bierwang gas field, Germany

Table 5 – Well-core φ-log(κ) data for Bierwang gas field formations

WELL #	Sample #	Z_{mn} (m)	Z_{mx} (m)	φ_{mn} (%)	φ_{mx} (%)	φ_{md} (%)	κ_{mn} (mD)	κ_{mx} (mD)	χ(%)	α	$\underline{\alpha\varphi}$
BWB4	56	1606	1624	7.2	31	26	0.11	2259	78	15.8	3.95
BW7	143	1521	1544	3.8	33	29	0.01	4100	86	16.2	4.51
BW15	60	1534	1541	2.8	32	30	2.26	9580	95	13.2	3.43
BW23a	342	1539	1596	4.4	31	25	0.29	4392	94	15.9	3.82
BW42	105	1678	1704	0.79	29	21	0.22	1202	94	16.0	3.08
BW52	237	1543	1579	9.5	36	27	0.18	3394	87	16.7	4.46
BWB5	81	2000	2044	15.2	34	24	3.05	3473	79	17.2	4.27
BWB4	165	1704	1775	12.1	29	25	10.2	632	98	9.86	2.43

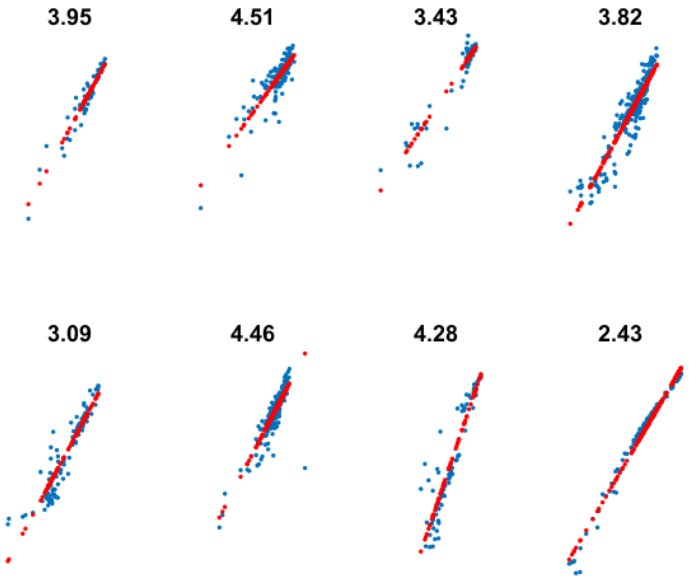

Figure 5 – Well-core φ-log(κ) linear relation for Bierwang gas field formations (Table 4); each subplot is titled with value αφ given by linear trend coefficient α and mean porosity φ.

2.5 Lewis shale reservoir analogue, Wyoming

Table 6 – Well-core φ-log(κ) data for Lewis shale analogue reservoir formation

WELL INTERVAL	Sample #	Z_{mn} (ft)	Z_{mx} (ft)	φ_{mn} (%)	φ_{mx} (%)	φ_{md} (%)	κ_{mn} (mD)	κ_{mx} (mD)	χ(%)	α	αφ
1	26	389	408	26	31	28	23.4	994	73	22.6	6.4
2	37	448	486	24	31	28	36.1	342	77	12.8	3.6
3	30	560	595	25	31	27	41.6	417	87	10.5	2.9
4	38	856	894	23	32	29	51.2	916	91	13.8	4.0

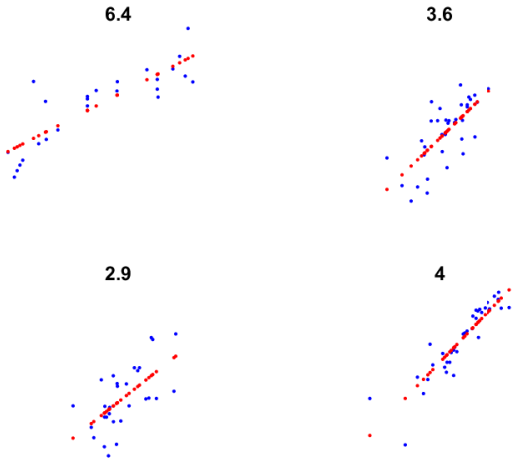

Figure 6 – Well-core φ-log(κ) linear relation for Lewis shale reservoir analogue formation (Table 5); each subplot is titled with value αφ given by linear trend coefficient α and mean porosity φ.

4. EVIDENCE FOR $\underline{\alpha\varphi}$ ~ 1.5-3.5 IN CRYSTALLINE ROCK

The abundance of well-core evidence for crustal reservoir poroperm systematics $\delta\varphi \propto \delta\log\kappa$ [2-3] and $\kappa \propto \exp(\alpha\varphi)$ [4] in porosity range $.03 < \varphi < 0.3$ is not replicated for crystalline basement rock with porosity range $\varphi < 0.01$. The relation $\delta\varphi \propto \delta\log\kappa$ is examined for suite of 31 well-core poroperm data for the KTB, Germany, deep well between 4 and 6 km (Appendix 2). The KTB data are particularly relevant, both because the well-core data format is similar to the crustal reservoir poroperm data format, and because KTB well-logs clearly indicate that spatial fluctuation power-spectral trend $S(k) \propto 1/k^1$ persists unabated to 8-9 km depths [25]. Analysis of KTB poroperm data is followed by a more general analysis of crystalline rock poroperm data from the Borrowdale Volcanics formation adjacent to the Sellafield nuclear facility in Cumbria, UK, investigated as a prospective nuclear waste repository [26-28].

Both the KTB and Sellafield data sets clearly indicate that, despite the order of magnitude lower porosity, $\varphi < 0.01$, crystalline rock maintains a good approximation the crustal reservoir norm, $\underline{\alpha\varphi}$ ~ 3-4**.** In establishing this result, it becomes plausible that the crustal rock-fluid interaction environment active at crustal reservoir depths to 5km does not disappear with below 5km in response to increasing confining pressure, reduced porosity, and retirement of mobile crustal fluids into hydrated minerals. It is thus plausible that understanding of the spatial-correlation mechanics of the highly-documental naturally occurring crustal rock-fluid interaction of hydrocarbon reservoir systems can be effectively transferred to basement rock. In particular, these systematics indicate that increasing crustal depth does not translate into decreasing or vanishing spatial-correlation heterogeneity, explicitly countering the standard notion that rock-fluid interactions become quasi-uniform at depth.

The KTB well poroperm data recovered from well intervals spanning 4 to 6 km depths are divided into four orientations with respect the wellbore axis and rock fabric. Core denominations are 's' and 'p' for core perpendicular and parallel to rock fabric, and 'a' and 'r' for core axial and radial with respect to the wellbore. Figure 7 compares the spatial correlation of fluctuations in well-core porosity (blue) and logarithm of permeability (red) for the four well-core orientations. Each data trace is expressed in zero-mean/unit-variance format.

The degree of spatial correlation for the Figure 7 poroperm sequences are respectively 66%, 68%, 69% and 74%. Taken alone, the observed poroperm spatial correlation values are suggestive but are not statistically significantly relative to the null hypothesis that these correlation values are the product of random chance. A second datum, however, greatly increases the statistical significance of the sequence spatial correlations: for each Figure 7 trace pair, the maximum correlation occurs at zero lag. Simulating Figure 7 for 100,000 instances of gaussian random numbers instead of KTB poroperm data indicates that there less than 1 part in a million chance that the quartet of Figure 7 zero-lag correlation values are the product of pure chance.

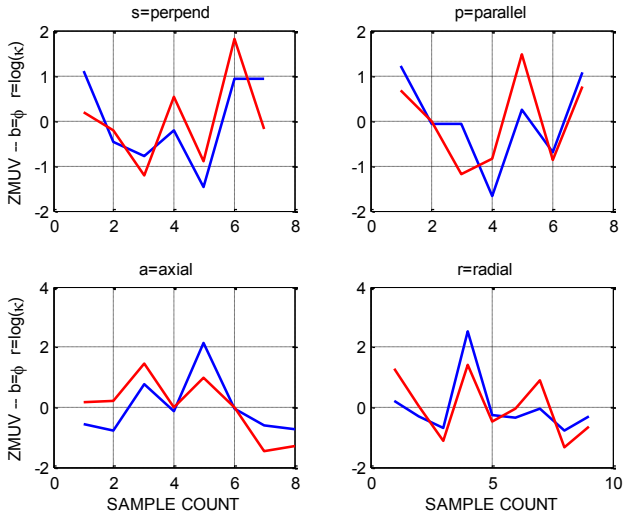

Figure 7 – KTB well-core spatial correlation $\delta\varphi \propto \delta\log(\kappa)$; zero-mean/univariance format; φ =blue, $\delta\log(\kappa)$ = red; well-core from depth interval 4-6km (Appendix 2).

Figure 8 evaluates the slope of the φ – logκ linear relation for the four KTB well-core orientations. Aside from a single point of porosity above 2%, the results of the linear fits give values of slope α as 320, 330, 99 and 280 respectively. If the data re restricted porosities less than 1%, then the slope α ~ 99 increases to α ~ 300. In light of the infrequency of porosities above 1%, it may transpire that the higher porosities are the result of the core being somewhat fractured, either naturally or by the coring process. From Figure 8, we can conclude that KTB deep crystalline rock appears to be characterised by values of α that are an order of magnitude greater than the values of α for crustal reservoir rock with porosities an order of magnitude greater. As each the quartet of KTB core samples has mean porosity ~ 0.5%, KTB well-core are characterised by poroperm product parameter value $\underline{\alpha\varphi}$ ~ 1.5.

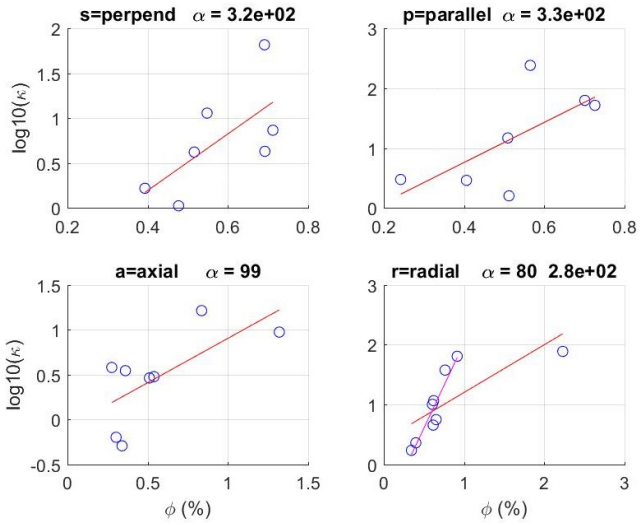

Figure 8 – KTB well-core relation $\kappa \propto \exp(\alpha\varphi)$; data blue circles; exponent fit for poro-connectivity parameter α (red); well-core from depth interval 4000m-6000m (Appendix 2). Omitting the two poroperm data with porosity greater than 1%, gives mean value α ~ 300 and poroperm product parameter value $\underline{\alpha\varphi}$ ~ 1.5.

A suite of well-scale permeability and well-to-well connectivity data were acquired at the UK nuclear waste disposal test site at Sellafield in Cumbria [26-28]. The geological unit investigated was the Borrowdale Volcanic Group (BVG) of metamorphosed Ordovician volcanics which outcrops to form the 50km by 50km area of 1000m topographic relief in England's Lake District. Figure 10 shows normal probability distributions for 50-meter well-interval hydraulic conductivities acquired during and after drilling. Figure 11 shows BVG well-core samples porosity distributions. The Figure 10 data format is that of 'normal probability', in which a straight-line trend implies a normal distribution for the variable plotted along the x-axis. As the plotted variable in Figure 9 is the logarithm of the observed hydraulic conductivity K [m/s], the data show that over five decades of hydraulic conductivity the BVG formation has a lognormal distribution of hydraulic conductivity.

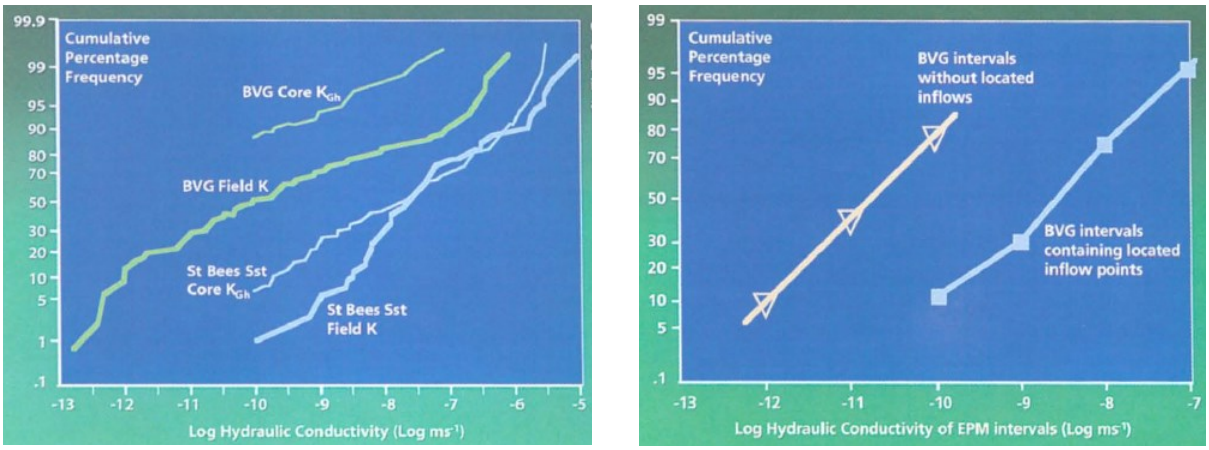

Figure 9 -- Normal probability plots of post-drilling wellbore flow test data (left) and while-drilling wellbore flow test data (right) for the Sellafield Rock Characterization Project in the Borrowdale Volcanics Group (BVG), Cumbria, UK [26].

The Figure 9 left-hand normal probability plot covers extensive post-drilling flow tests designated FST (full sector test) [27]. The right-hand normal probability plot covers the more limited EPM (environmental pressure measurement) conducted over 50 meter intervals during drilling operations. Permeability κ [m^2] is linearly related to hydraulic conductivity through the factor $\mu/\rho g \sim 10^{-7}$m·s, $\kappa = K \mu/\rho g$, for the dynamic viscosity of water $\mu \sim 10^{-3}$Pa·s, density of water $\rho \sim 10^3$kg/m^3, and acceleration of gravity $g \sim 10 m^2/s$. BVG field-scale permeability ranges from $\kappa \sim 10^{-19}m^2$ to $\kappa \sim 10^{-14}m^2$, with measured well-core permeability between $\kappa \sim 10^{-17}m^2$ to $\kappa \sim 10^{-14}m^2$. Higher and lower values of field-scale permeability, appearing in the parts of the distribution that deviate from a straight-line trend, represent outliers of increasingly sparse sample numbers. Field-scale permeability is observed to divide into two categories: flow volumes without evidence of faults/fractures, $\kappa \sim 10^{-19}m^2$ to $\kappa \sim 10^{-17}m^2$, and flow volumes with evidence of faults/fractures, $\kappa \sim 10^{-17}m^2$ to $\kappa \sim 10^{-14}m^2$.

We can relate BVG permeability to BVG porosity through the empirical expression $\kappa \approx \underline{\kappa}\ exp(\alpha(\varphi - \underline{\varphi}))$. Figure 10 indicates BVG porosity data in terms of observed failure types under uniaxial compression [28]. An order of magnitude estimate BVG porosity is $\varphi \sim 1\%$ with minimum value $\underline{\varphi} \sim 0.1\%$

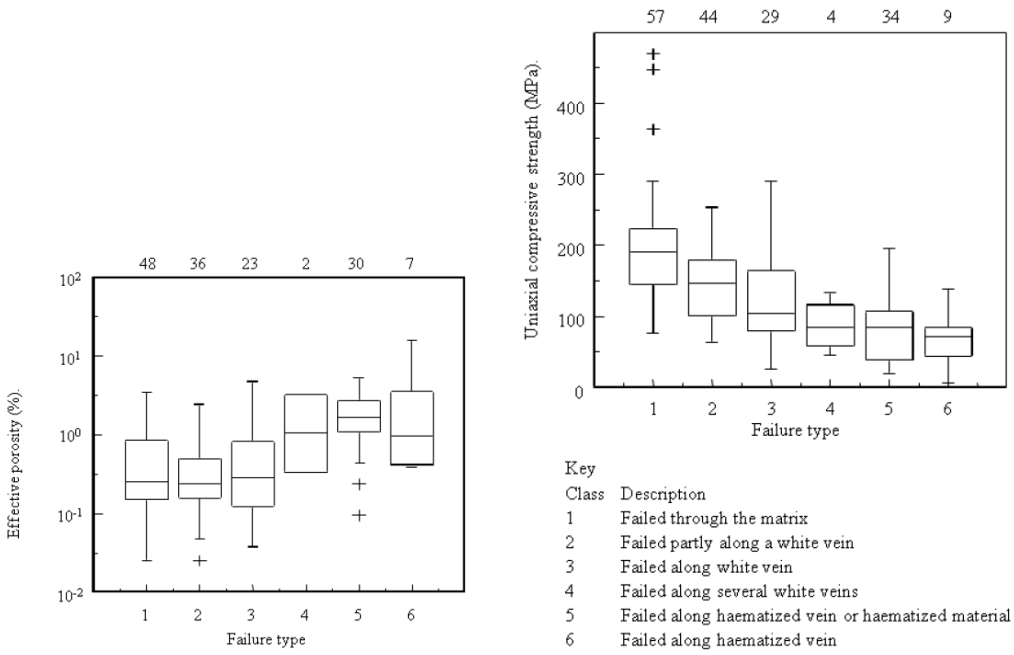

Figure 10 – Porosity and uniaxial compression test data for BVG well-core, Sellafield, Cumbria, UK [28].

Using the poroperm relation with adjusted parameter values for κ, φ and α, Figure 11 plots show simulated field-scale hydraulic conductivity normal probability distributions. For a permeability field generated by a Gaussian distribution of 150 core samples with minimum porosity ~ 0.03% and maximum porosity ~ 1%, the observed hydraulic conductivity distributions have best-fit poroperm-connectivity parameters values $\alpha \sim 1000$, 600 and 700 for plots left to right.

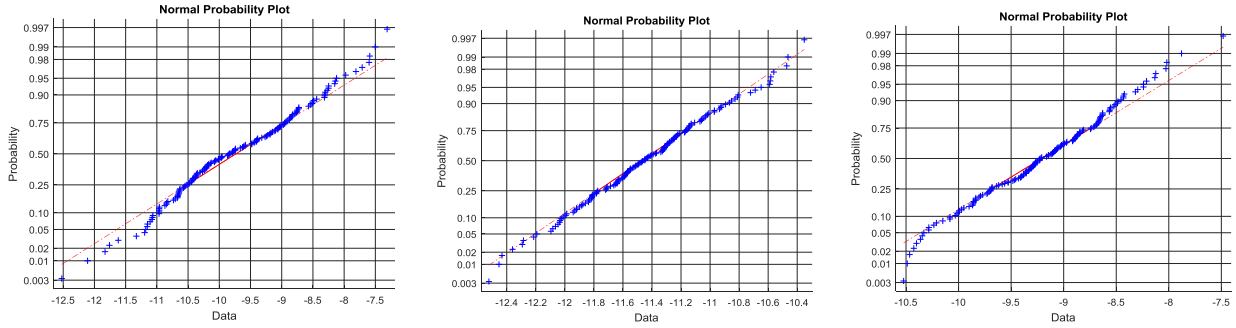

Figure 11 -- Synthetic normal probability plots for hydraulic conductivity fitting BVG post-drilling FST wellbore flow data. Fitting the synthetic plots to a normal distribution of porosity in the porosity range of Figure 10 generates the plotted normal probability distributions for values of α 1000, 600 and 700, respectively.

The EPM BVG field-scale permeability distribution data imply a minimum permeability $\kappa \sim 3\ 10^{-20} m^2$ for crustal volumes with no evidence of passing fluid through extent fracture structures, and a minimum BVG permeability $\kappa \sim 3\ 10^{-18} m^2$ for crustal volumes with evidence of passing fluid through extent fracture structures. The Figure 11 implied values of poroperm connectivity parameter α inferred from observed well-scale flow data constrained by observed well-core porosity data are, respectively, 1000, 500 and 700. Taking mean BVG porosity to be $\varphi \sim 0.6\%$, the characteristic $\underline{\alpha\varphi}$ value for the BVG crystalline rock is $\underline{\alpha\varphi} \sim 4.6 \pm 1.2$.

5. ISING MODEL INTERPRETATION OF CRUSTAL ROCK-FLUID COUPLING PARAMETER $\underline{\alpha\varphi} \sim 3\text{-}4$

Figure 1 illustrates the macroscopic spatial correlation systematics of the Ising model system of interacting microscale elements. According to the Ising model mathematical structure, three types of spatial correlation necessarily exist [6]. As as a function of system temperature $\underline{\theta}$ in relation of a critical state temperature $\underline{\theta}_{crit}$, the three spatial correlation states are:

- Uncorrelated or gaussian 'white noise' spatial randomness, which occurs when the system temperature $\underline{\theta}$ is higher than the system critical temperature, $\underline{\theta} > \underline{\theta}_{crit}$; the corresponding well-log spatial frequency power spectrum is flat, $S(k) \propto 1/k^0$.
- Strongly correlated 'red noise' spatial randomness, which occurs when the system temperature $\underline{\theta}$ is lower than the system critical temperature, $\underline{\theta} < \underline{\theta}_{crit}$; the corresponding well-log spatial frequency power spectrum scales as $S(k) \propto 1/k^2$.
- Intermediate correlated 'pink noise' spatial randomness, which occurs when the system temperature $\underline{\theta}$ is near the system critical temperature, $\underline{\theta} \sim \underline{\theta}_{crit}$; the corresponding well-log spatial frequency power spectrum is $S(k) \propto 1/k^1$.

Empirically, the spatial fluctuation properties of the crustal rock-fluid interaction system correspond to the last of these three spatial fluctuation options, with well-log spatial fluctuation power spectra observed worldwide to scale with spatial frequency k as $S(k) \propto 1/k^1$ [1] This essentially universal aspect of crustal rock-fluid interaction is accompanied by the empirical condition that well-core and well-flow data indicate that the observational parameter $\underline{\alpha\varphi}$ is observed to occur in a narrow range of values, $\underline{\alpha\varphi} \sim$ 3-4, derived from the well-core poroperm relation, $\log\kappa \sim \alpha\varphi$ across for a range of geological settings that span two decades of rock porosity value, $.003 < \varphi < 0.3$ [2-3]. Values of order $\underline{\alpha\varphi} \sim$ 3-4 are consistent with the observation that crustal reservoir fluids worldwide are lognormally distributed as given by the empirical relation $\kappa \propto \exp(\alpha\varphi)$ [4].

By analogy with Figure 1 spatial correlation systematics, it would appear that $\underline{\alpha\varphi} \sim$ 3-4 represents a critical-state condition for microscale energetics of the crustal rock-fluid interaction. Making this analogy allows us to interpret the observed values of well-core sequence and field-scale flow data $\underline{\alpha\varphi}_{crit} \sim$ 3-4 as equivalent to the mathematically-mandated critical system temperature $\underline{\theta}_{crit}$ at which the Ising model phase transition takes place and long-range spatial correlations naturally emerge from the otherwise short-range thermal interactions.

To explore this identification, we first note how the internal properties of the Ising system are applied to the standard statistical mechanical treatments of ferromagnetism and the lattice gas phase transition [5-6]. We then generalise the standard statistical mechanics to incorporate a wider range of system element interaction energy processes that accommodates the empirical crustal rock-fluid interaction condition $\underline{\alpha\varphi}_{crit} \sim$ 3-4 [7-8]. In the background of any discussion of physical system analogues for the Ising model lies the mathematical demonstration that the Ising model interpreted in terms of the 2nd law of thermodynamics *necessarily* has a critical temperature that marks a phase change between essentially uncorrelated system randomness and highly correlated system randomness [5-6]. The crustal rock-fluid interaction spatial correlation empirics thus seem likely to arise from a deeply fundamental physical process linking crustal rock-fluid microscale energetics to crustal rock-fluid macroscale spatial correlations.

5.1 Statistical mechanics of Ising model ferromagnetic and lattice gas phase transitions

The kinetic energy of atoms and molecules in solids, liquids and gases (along with the historically important electromagnetic field energy coupled to atoms and molecules) is a fundamental and pervasive energy reservoir that can profoundly affect the energy distribution within material systems. The 1st law of thermodynamics states that the energy of a material system and its environment is conserved. The 2nd law of thermodynamics states that the 'heat energy reservoir' effect on material system energy distribution forces the system to go from a less probable more ordered state to a more probable less ordered state. The more probable state is less spatially organised state; i.e., thermal systems evolve from more internal order to less internal order. Under the 2nd law constraint, the interaction energetics of atoms, molecules, and their larger-scale assemblages such as mineral grains and associated cements, are effectively taxed by irreversibly leaking part of their interaction energy to an ever-present 'heat bath' energy reservoir. Universally, the state of the 'heat bath' energy reservoir is associated with a temperature T corresponding to the mean-kinetic energy of the constituent atoms and molecules (and potentially an associated electromagnetic field). In some cases, however, the role of system structure 'information' is entrained in the dynamics of internal energy organization.

Given the pervasive nature of the thermal process constraint of the 'heat bath' of ambient thermal energy reservoir, it should be no particular surprise that crustal rock-fluid interaction energetics are influenced by the temperature of the crustal 'heat bath'. What can be extremely surprising, however, is the intricate coupling between the system elements and their 'heat bath' energy reservoir. It is the genius of the Ising model to manifest in simple terms the strange and wonderful interaction between the Ising model system elements and the 'heat bath' temperature in the presence of which the Ising system elements exchange their interaction energy. With the Ising model as guide, it is possible to associate lattice system energetics with a more general manifestation of the 2nd law of thermodynamics expressed in terms of a more general concept of the 'heat bath' energy reservoir. This generalisation gives physical meaning to the crustal rock-fluid interaction empirical datum $\underline{\alpha\varphi}_{crit} \sim$ 3-4.

In 1877, Boltzmann interpreted the existing expressions of the 2nd law of thermodynamics in terms of the probability p_i of a given energy state ε_i for the i^{th} element in a physical system at thermal equilibrium temperature T,

$$p_i = \exp(-\varepsilon_i/k_B T) \,/\, \sum_{i=1\ldots N} \exp(-\varepsilon_i/k_B T), \qquad (1)$$

where $k_B = R/N_{AV}$ is Boltzmann's constant fixed by the observed properties of gases interpreted by the ideal gas law $PV = RT$ and measurement of Avogadro's number N_{AV}, and probability ranges from 0 to 1.

The total energy of the system is the sum over all element energies ε_i weighted by the energetics weight factor $\exp(-\varepsilon_i/k_B T)$,

$$E = \sum_{i=1\ldots N} \varepsilon_i \exp(-\varepsilon_i/k_B T). \qquad (2)$$

The parallel sum

$$S = \sum_{i=1...N} p_i \log(p_i) = -1/k_B T \sum_{i=1...N} p_i \varepsilon_i \quad (3)$$

is the system parameter entropy S that links the probability p_i of a site energy value to the site energy magnitude ε_i. In these functions of site energy magnitude and site energy probability, the role of system temperature T as a measure of the thermal energy heat bath energy reservoir is fundamental.

The Ising system model assigns one of two energy states ε_i, i = 1,2, to each node in a 2d or 3d lattice of N nodes. The Ising model thermodynamic state is thus expressed explicitly by counting the nodes in the two energy states. For a physical assemblage of iron atom magnetic dipoles of magnitude m with nodal 'spin states' s_i that are either +1 or -1, the macroscopic observable mean magnetic moment $\underline{M}$ is the parallel of system energy (2),

$$\underline{M} = m \sum_i s_i \exp(-\varepsilon_i/k_B T). \quad (4)$$

In the absence of an external magnetic field to orient the atomic dipoles, it is logical to expect that there is no preferred atomic alignment direction for any system temperature $\underline{\theta}$, as the sum (4) over nodal states can be expected to have as many +1 alignments as -1 alignments, the giving $\underline{M} \sim 0$ [5]. This expected nodal state spatial distribution is illustrated in Figure 1 by the left-hand disordered 'white noise' Ising model state. Applied to crustal rock-fluid interactions, it is similarly logical that, in the absence on a particular internal interaction mechanism, the natural crustal rock state is the uncorrelated randomness of 'white noise' spatial fluctuations which can be averaged over in the sense of (4) giving mean magnetisation $\underline{M} \sim 0$.

The 'logic' of (4) is, however, defied by the phase transition behaviour of physical systems. As illustrated by the Ising model simulations in Figure 1, the mathematical model can generate long-range spatial distribution simulations of physical system behaviour that defy the $\underline{M} \sim 0$ expectation of (4). The phenomenon of ferromagnetism provides the physical evidence for energy states that violate expectation (4). The mathematical origin of the transition between short-range interactions (left-hand white noise distributions of Figure 1) and long-range interactions (center and right-hand pink noise and red noise distributions of Figure 1) was established in a 1935 mathematical analysis of Ising model behaviour [6].

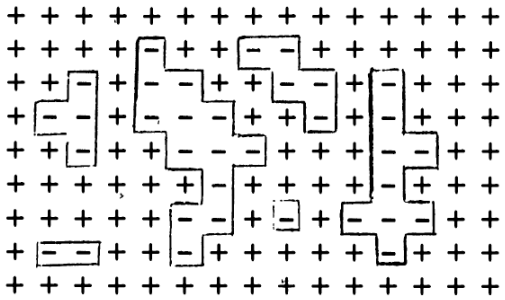

Figure 12 -- Ising 2d model spatial distributions of lattice nodal interaction-energy assuming that the boundary elements all exist in a '+' state [6]. While (4) implies there will be as many '-' states as '+' states in the interior of the Ising model lattice, it is proved that there exists a system temperature T_{crit} for which the probability of a '-' state is vanishingly small. It is thus guaranteed that the Ising model interior will have extended internal domains of '+' states in response to the ´boundary state of '+' elements.

In light of its profound insight into the cooperative long-range behaviour of short-range microscale interactions in 2d and 3d physical (and mathematical) systems, Figure 12 sketches elements of the 1935 mathematical demonstration for the 2d Ising system [6]. The demonstration posed the question of what would happen in a 2d Ising system if, by some minor external event, all edge nodes of a 2d Ising model lattice were in the same state. This boundary state is represented by '+' nodes states around the rim of the Figure 12 Ising lattice. The answer to this question was given by demonstrating that the lattice edge boundary state could allow the existence of essentially arbitrarily large internal structures of '-' lattice node, as indicated by the Figure 12 internal domains of collective '-' nodal states. The mathematical statement was, in the notation of (1)-(4), that the probability $P(s_i = -1)$ of a '-' nodal state at a given i^{th} node can be made arbitrarily small by system temperature T being sufficiently small,

$$P(s_i = -1) < \tfrac{1}{2} (4\exp(-\exp(-\varepsilon_i/k_B T))/(1 - 4\exp(-\exp(-\varepsilon_i/k_B T))^2. \quad (5)$$

By (5), there must be a system temperature T_{crit} for which the effect of a systematic '+' alignment of the Ising lattice boundary elements is to force the '-' alignment of an arbitrary interior element to be vanishingly small, implying that cooperative action between interior Ising lattice elements necessarily reduces the probability of an arbitrary element from the expected probability ½ to a collective element action probability approaching 0. Improbability of a '-' alignment necessarily means probability of a '+' alignment, hence cooperative action between elements exists throughout the Ising model interior.

Establishing the existence of a 2d Ising system temperature T_{crit} requiring the vanishing probability of Ising domains of '-' nodal states when the boundary nodal states were uniformly '+', left undetermined the value of the demonstrated temperature. A 1937 result indicated that the critical temperature T_{crit} for the 2d Ising model probability expression (5) obeyed the criterion [6]

$$T_{crit} = (1 - T_{crit}) / (1 + T_{crit}). \quad (6)$$

The celebrated Onsager 1944 complete mathematical analysis of the 2d Ising system for zero external magnetic field -- focusing entirely on the nodal interaction mechanics of the Ising lattice system -- confirmed the T_{crit} system temperature result (6) and provided grounds for describing how the 2d Ising lattice system generated long-range spatial correlation structures at the critical state system temperature T_{crit} through the existence of a singularity in the interior element-element spatial correlation length, $\xi \rightarrow \infty$ [5]. Long-range spatial correlation lengths lead directly to well-log spatial fluctuation power-law spectral scaling [1].

5.2 Generalised statistical mechanics for crustal rock-fluid interaction phase transition at $\underline{\alpha\varphi}_{crit} \sim$ 3-4

While we know with virtual certainty that the porosity state at any node in in a crustal rock-fluid interaction representation lattice is dependent on a site energy ε_i, we do not have means of measuring the crustal rock-fluid interaction site energy in the same way as we know the nodal site interaction energy of a spin-state of an iron atom. For a crustal rock-fluid interaction, it is not clear what physical measurement corresponds to the thermal energy of magnetic dipoles relative to a heat bath of temperature T. Crustal rock-fluid interactions require, therefore, a more general formulation of how microscale interaction energy is distributed macroscopically in the Ising lattice nodal system.

Jayne [7] developed such an formalism for the distribution of physical property energetics in an Ising lattice. The basis for Jaynes approach was established by Shannon's mathematical analysis of what has come to be called the entropy of information [8]. As permeability is a physical manifestation of pore-connectivity information, it is plausible to think of fluid permeability in a crustal rock granular assembly in terms of the information content of porosity connectivity that effectively defines permeability. Porosity-connectivity information in a physical system is fundamentally not available to the outside observer except through the probe of fluid permeability. Via the mechanics of information entropy, it is possible to establish a detailed energetics connection between observable discrete crustal rock-fluid interaction properties and otherwise unobservable internal flow connectivity structures.

Following Jayne [7], we suppose that we are able to measure a physical variable f that takes a series of values $\{f_i\}$ at $i = 1 \ldots\ldots N$ lattice sites. Our measurement information can then be formulated in terms of the value of f_i at the i^{th} lattice site and the probability $0 < p_i < 1$ of that value appearing at that site,

$$\langle f \rangle = \sum_i p_i f_i, \quad (7)$$

where probabilities are defined so as to sum to unity, $\sum p_i = 1$. Shannon [8] showed that a specific distribution of probabilities $H(p_1 \ldots p_N)$ formally allows for the greatest possible uncertainty of the probability distribution, corresponding to the maximum information system entropy:

$$H(p_1 \ldots\ldots\ldots p_N) = - \sum_i p_i \log(p_i). \quad (8)$$

A formal relation between p_i and f_i is established by maximising $H(p_1 \ldots\ldots\ldots p_N)$ under the constraints that $\langle f \rangle = \sum_i p_i f_i$ and $\sum p_i = 1$. The maximisation procedure by Lagrange multipliers gives the probabilities p_i as

$$p_i = exp(-\alpha f_i)/Z(\alpha), \quad (9)$$

where Lagrange multiplier α is an integration parameter and $Z(\alpha)$ is the normalising sum of all energy-expectation terms $exp(-\alpha f_i)$,

$$Z(\alpha) = \sum_i exp(-\alpha f_i). \quad (10)$$

The observed physical property $\langle f \rangle$ is then defined in terms of nodal values f_i and nodal state probabilities p_i,

$$\langle f \rangle = - \partial log(Z(\alpha))/\partial\alpha = -1/Z \; \partial Z(\alpha)/\partial\alpha = \sum_i f_i \, exp(-\alpha f_i)/Z = \sum_i p_i f_i. \quad (11)$$

Applying this physical property analysis to Ising nodal porosity φ gives probability distribution for each nodal porosity φ_i,

$$p_i = exp(-\alpha\varphi_i)/Z. \quad (12)$$

As the interaction energy-controlled probability p_i for a given value of porosity φ_i at the i^{th} Ising model node is a good proxy for permeability, (12) essentially reproduces the observed empirical relation between permeability and porosity,

$$\kappa_i = exp(-\alpha\varphi_i). \quad (13)$$

Comparing (13) with (1)-(3), it is seen that the Lagrange multiplier integration constant α assumes the desired role of an equivalent to temperature for the crustal rock-fluid interaction that links nodal energy to nodal information about porosity-connectivity in the Ising system. With (12)-(13), we can identify the Lagrange multiplier parameter α of (7)-(12) with the observed crustal rock-fluid interaction process empirical parameter condition $\underline{\alpha\varphi} \sim$ 3-4 derived from (13) and the above displayed crustal formation poroperm data for $\log\kappa \sim \alpha\varphi$.

From the vantage point of (12), we may view crustal permeability as a manifestation of porosity probability for crustal rock-fluid flow at a given nodal site. It makes physical sense that the greater the probability of porosity at a lattice nodal site the greater the probability of

interactive fluid flow between the given node and nearby nodes. Put differently, permeability is a form of information about how pores connect, and pore connectivity is a form of information about spatial correlation of a pore population.

On the basis of the parallel between the general mathematical and computational model thermodynamic system (12) and the empirical poroperm relation (13), we can understand the above established empirical relation $\underline{\alpha\varphi}_{crit}$ ~ 3-4 as physical statement about the crustal rock-fluid interactions that extend from standard reservoir rock with $0.03 < \varphi < 0.3$ to deep seated crustal basement rock with an order of magnitude lower porosity, $0.003 < \varphi < 0.03$. For a given crustal rock volume, the parameter α takes values such that the mean porosity $\underline{\varphi}$ for that rock volume gives $\underline{\alpha\varphi}$ ~ 3-4. We then observe that empirical $\underline{\alpha\varphi}$ ~ 3-4 values correspond to a pervasive crustal rock state in which long-range spatial correlation spectral systematics $S(k) \sim 1/k$ occur at scale lengths corresponding to spatial frequencies $1/\text{km} < k < 1/\text{cm}$. The Ising model lattice node construct also indicates that the $\underline{\alpha\varphi}$ ~ 3-4 empirical crustal rock state represents a phase change between high mean porosity disaggregated rock in the uppermost crust, and low mean porosity ductile flow rock in the lower crust.

6. CONCLUSIONS -- ROCK-FLUID COUPLING PARAMETER $\underline{\alpha\varphi}$ ~ 3-4 FOR BASEMENT FLOW STIMULATION

Our discussion of crustal rock-fluid interaction in terms of the Ising model gives a plausible physical basis for the four widely-observed naturally-occurring crustal flow properties, with well-log spatial correlation evidence that the signature spatial correlation properties persist in crystalline basement conditions to at least 8km depth [25]:

i. Well-log spatially-correlated fluctuations characterised by power-law spectral scaling $S(k) \propto 1/k^1$ over scale range $\sim 1/\text{cm} < k < \sim 1/\text{km}$;
ii. Well-core sequence spatial variations in porosity that correlate with spatial variations in the logarithm of permeability, $\delta\varphi \propto \delta\log\kappa$, over m-Hm scale lengths;
iii. Lognormally distributed well productivity, $\kappa \propto \exp(\alpha\varphi)$, for groundwater, conventional and unconventional hydrocarbons, and geothermal fluids, along with fossil flow system mineral deposits;
iv. Ising model statistical mechanics support for a 'critical state' parameter $\underline{\alpha\varphi}_{crit}$ explaining (i)-(iii) in terms of maximum information entropy for the rock-fluid interaction system.

It is of interest to consider the implications that these pervasive naturally-occurring crustal rock-fluid interaction properties have for stimulating basement rock to achieve commercial rates of heat energy extraction for wellbore-to-wellbore flow. It can be calculated that a properly stimulated crustal volume enclosing a 3-km-long horizontal well-pair with 30-50-meter offset can supply a district heating plant with 25kg/s flow of 100°C fluid for 30 years [25]. Compared with past projects to extract heat from crustal basement rock [17-22], a 3km-long 30-50m offset horizontal wellbore-pair is modest in both spatial extent and fluid flow rate. We note, however, that past projects were based on creating Hm-scale planar 'cubic-law' fluid flow structures in rock assumed to have effectively uniform in mechanical properties [18-20]. These crustal stimulation projects have failed create the necessary flow structures [23-24].

Approaching wellbore-to-wellbore flow stimulation on the Ising-model-based poroperm relation (13), $\kappa_i = exp(-\alpha\varphi_i)$, and/or its equivalent well-core empirical relations (ii), $\delta\varphi \propto \delta\log\kappa$, and (iii), $\kappa \propto \exp(\alpha\varphi)$, as representative of fundamental crustal poroperm properties, we can focus on individual porosity sites as key to the crustal flow stimulation process. More particularly, we can look at the energetics of creating a small change in porosity, or, prospectively, a small change in associated value of α that governs porosity-connectivity.

The porosity of a unit rock volume is given by the number n of grain-scale defects associated with the pores. As above, we let grain-scale defects be cement bond failures that allow pores to communicate their fluid content with adjacent pores. As pores have the lowest elastic modulus, they are subject to the greatest local strains within a crustal volume undergoing deformation. For a sample rock volume with n defects, spatial connectivity between defects within the sample scales as the combinatorial factor $n! = n(n\text{-}1)(n\text{-}2)(n\text{-}3)\ldots\ldots 1$. By Stirling's law, $\log(n!) \sim n(\log(n)\text{-}1)$, the effect of incrementing the defect population of a sample volume by a small number $\delta n << n$, $n \rightarrow n + \delta n$, is to increment permeability as $\delta\log(n!) = \log((n+\delta n)!) - \delta\log(n!) \sim (n+\delta n)\log(n+\delta n) - 1) - n(\log(n)\text{-}1)$, or $\delta\log(n!) \sim \delta n \log(n)$, thus duplicating empirical property (ii), $\delta\varphi \propto \delta\log(\kappa)$.

This pore-node-based construct quantifies the effect on inter-granular fluid flow of introducing a single grain-scale defect into a poroperm structure, $n \rightarrow n + 1$. For a fluid of dynamic viscosity μ driven by pressure gradient P', Poiseuille volumetric flow per unit breadth of the flow front is $Q\ [\text{m}^2/\text{s}] = P'\,\Delta^3/12\mu\ [\text{Pa/m m}^3/\text{Pa·s}]$. The corresponding fluid velocity is $v\ [\text{m/s}] = P'\,\Delta^2/12\mu$. For a gap Δ comprising a number n defects in the continuum flow structure, the mean gap increment is $\delta\Delta \sim \Delta/n$. It follows from $(v + \delta v)/v = 1 + \delta v/v = (\Delta + \delta\Delta)^2/\Delta^2 \sim 1 + 2\delta\Delta/\Delta$, that adding a single defect to the medium increases the gap by $\Delta\delta$ and increases fluid velocity by $\delta v/v \sim 2/n$.

For the disseminated empirical granular medium with fluid velocity $v \propto \exp(\underline{\alpha\varphi})$, the equivalent increment gives $(\kappa + \delta\kappa)/\kappa = 1 + \delta\kappa/\kappa \propto \exp(\delta\underline{\alpha\varphi}) \sim 1 + \delta\underline{\alpha\varphi}$, whence for $\underline{\varphi} = n\delta\varphi$, $\delta\kappa/\kappa = \delta v/v \sim \delta\underline{\alpha\varphi} = \underline{\alpha\varphi}/n$. For standard reservoir formations with porosity in the range $.1 < \varphi < .3$, the empirical values of α, $20 < \alpha < 40$, give $\underline{\alpha\varphi}$ ~ 3-4 fluid velocity increment factor for aquifer formations. For basement rock with porosity an order of magnitude smaller, $\varphi \sim .0075$, the value of α increases by an order of magnitude, $300 < \alpha < 700$, giving an empirical estimate of fluid velocity increment factor $\underline{\alpha\varphi} \sim 3$ for basement formations.

Creating a grain-scale defect in a crustal volume produces greater flow effect if the defect is embedded in a granular percolation flow structure than if the defect contributes to a conduit gap in the smooth continuum flow structures of the discrete fracture concept of EGS

stimulation. It follows that energy expended by wellbore pressurization is more effective in dissipating wellbore fluid pressure fronts if defects generated by fluid pressures contribute to granularity flow structures than if they contribute to continuum flow structures. Given the extensive evidence of well-log, well-core, and well-flow empirics (i)-(iv) as the ambient condition of crustal rock, we may argue that wellbores penetrating crustal media will typically encounter localised disseminated/granularity rather than planar geometric/continuum flow surfaces associated with discrete fracture displacement structures. On the basis of this probability argument, we can interpret wellbore-accessible temperature data as evidence of heat transport by flow in spatially-correlated grain-scale poroperm connectivity structures consistent with the Ising model of long-range node-node interactions [25].

We can further argue that the ambient crustal empirics (i)-(iv) result from the implied energetics of defect insertion through rock-fluid interaction. Rock stress involving fluids is more easily dissipated if fluid permeability stimulation proceeds through spatially-correlated fracture-connectivity granularity rather than through spatially-uncorrelated effective-medium planar continuum displacements. For generating ambient crustal fluid-rock flow conditions, the fact that porosity increments require doing work against confining stresses means that it is energetically favourable for defect enhancement to proceed in a spatially-correlated granularity medium than in a spatially-uncorrelated continuum medium. Discrete fracture systems may thus be seen to characterize crustal tectonic settings in which solid-rock displacement rates due to far-field tectonic plate motion exceed the rate at which fluid pressures can dissipate through slower fracture-connectivity mechanisms. EGS mechanisms based on local wellbore-centric fluid pressurization rather than elastic stress generated by far-field tectonics may thus couple more readily to the slower ambient-crust defect injection processes leading to spatially-correlated granularity than to the faster defect injection processes leading to discrete-fracture displacements.

REFERENCES

[1] Leary PC. Fractures and physical heterogeneity in crustal rock, in *Heterogeneity of the Crust and Upper Mantle – Nature, Scaling and Seismic Properties*, JA Goff & K Holliger eds., Kluwer Academic/Plenum Publishers, New York, **2002**, 155-186.

[2] Leary PC & Al-Kindy F (2002) Power-law scaling of spatially correlated porosity and log(permeability) sequences from northcentral North Sea Brae oilfield well core, *Geophysical Journal International 148*, 426-442.

[3] Leary P, Malin P & Niemi R (2017a) Finite-Element Modelling of Wellbore-Observed Fracture-Borne Heat Advection – Application to EGS Stimulation in Basement Rock, *41st Workshop Geothermal Reservoir Engineering*, Stanford University, February 13-15, SGP-TR-212; Leary P, Malin P & Niemi R (2017b) Fluid flow & heat transport computation for power-law scaling poroperm media, *Geofluids*, Volume 2017, https://doi.org/10.1155/2017/9687325

[4] Malin P, Leary P, Shalev E, Rugis J, Valles B, Boese C, Andrews J & Geiser P (2015) Flow Lognormality and Spatial Correlation in Crustal Reservoirs: II – Where-to-Drill Guidance via Acoustic/Seismic Imaging, WGC2015, 19-24 April, Melbourne AU.

[5] Chandler D (1987) *Introduction to Modern Statistical Mechanics*, Oxford University Press

[6] Cipra BA (1987) An Introduction to the Ising Model, *The American Mathematical Monthly*, Vol. 94, No. 10. (Dec., 1987), pp. 937-959; http://links.jstor.org/sici?sici=0002-9890%28198712%2994%3A10%3C937%3AAITTIM%3E2.0.CO%3B2-V

[7] Jaynes ET (1957) Information theory and statistical mechanics, *Physical Review*, V106, No4, 620-630.

[8] Shannon CE (1948) A Mathematical Theory of Communication, Reprinted with corrections from *The Bell System Technical Journal,* Vol. 27, pp. 379–423, 623–656, July, October, 1948.

[9] Theis CV (1935) The relation between the lowering of the piezometric surface and the rate and duration of discharge of a well using ground-water storage, *Transactions of the American Geophysical Union*, Part 2, 519-524, August 1935; DOI: 10.1029/TR016i002p00519.

[10] Muskat M (1937) The Flow of Homogeneous Fluids Through Porous Media, McGraw-Hill, pp763.

[11] Hubbert MK (1941) Motion of ground water, *Transactions of the New York Academy of Sciences, Series II No 3*, 39-55.

[12] Hubbert MK (1957) Darcy's law and the field equations of the flow of underground fluids, *International Association of Scientific Hydrology, Bulletin*, *2:1*, 23-59; doi: 10.1080/02626665709493062.

[13] Bear J (1972) *Dynamics of fluids in porous media*, American Elsevier, New York.

[14] Jaeger JC, Cook NGW & Zimmerman RW (2007) Fundamentals of Rock Mechanics, Blackwell Publishing, pp475.

[15] Ingebritsen S, Sanford W & Neuzil C (2006) *Groundwater in Geological Processes*, Cambridge University Press, pp536.

[16] Mavko G, Mukerji T, & Dvorkin J (2009) *The Rock Physics Handbook*, Cambridge University Press., pp511

[17] Tester JW et al (2006) The Future of Geothermal Energy, Impact of Enhanced Geothermal Systems (EGS) on the United States in the 21st Century, http://geothermal.inel.gov.

[18] Gringarten AC, Witherspoon PA & Ohnishi Y (1975) Theory of heat extraction from fractured hot dry rock, *Journal of Geophysical Research*, 1120-1124.

[19] Wunder R & Murphy H (1978) Singly and multiply fractured hot dry rock reservoirs, Los Alamos National Laboratory Report, LA-7219-MS, UC-66a, 1-15.

[20] Sutter D, Fox DB, Anderson BJ, Koch DL, Von Rohr PF, Tester JW (2011) Recovery in a Model EGS Fractured Reservoir, 36th Workshop on Geothermal Reservoir Engineering, Stanford Geothermal Program Workshop Report SGP-TR-191

[21] Hasting M, Albaric J, Oye V, Reid P, Messeiller M, Llanos E, Malin P, Shalev Hogg M, Alvarez M, Miller A, Walter C, Boese C & Voss N (2011) Real-Time Induced Seismicity Monitoring During Wellbore Stimulation, Australian Geothermal Energy Conference;
https://www.geothermal-energy.org/pdf/IGAstandard/AGEC/2011/GA20050.pdf

[22] Bendall B, Hogarth R, Holl H, McMahon A, Larking A & Reid P (2014) Australian Experiences in EGS Permeability Enhancement – A Review of 3 Case Studies, 39th Workshop Geothermal Reservoir Engineering, Stanford University, SGP-TR-202.

[24] Moeck IS (2014) Catalog of geothermal play types based on geologic controls, *Renewable and Sustainable Energy Reviews 37*, 867–882.

[23] Moeck IS & Beardsmore G (2014) A new 'geothermal play type' catalog: Streamlining exploration decision making, 39th Workshop Geothermal Reservoir Engineering, Stanford University, SGP-TR-202.
[25] Leary P, Malin P, Saarno T & Kukkonen I (2017) Prospects for Assessing Enhanced Geothermal System (EGS) Basement Rock Flow Stimulation by Wellbore Temperature Data, *Energies*, vol 10 , no. 12, DOI: 10.3390/en10121979.
[26] Chaplow R (1996) The geology & hydrology of Sellafield: an overview, *Quarterly Journal of Engineering Geology 29*, S1-12; doi: 10.1144/GSL.QJEGH.1996.029.S1.01.
[27] Sutton JS (1996) Hydrogeological testing in the Sellafield area, *Quarterly Journal of Engineering Geology 29*, S29-38; doi: 10.1144/GSL.QJEGH.1996.029.S1.03.
[28] Entwisle DC, Hobbs PRN, Jones LD, Gunn D & Raines MG (2003) The relationships between effective porosity, uniaxial compressive strength and sonic velocity of intact Borrowdale Volcanic Group core samples from Sellafield, GEGE2166-RAD, nora.nerc.ac.uk/504073/1/NIREX_paper_2003%20(2).pdf.

APPENDIX 1 -- MATLAB CODE FOR 2D ISING MODEL LATTICE ENERGY SPATIAL DISTRIBUTIONS

```
% Metropolis algorithm for Ising model configuration of spins with coupling coefficient |J| at temperature |kT|.
%|spin| is a matrix of +/- 1's.
% Copyright 2017 The MathWorks, Inc.
numIters = 2^8 * numel(spin);
for iter = 1 : numIters
   % Pick a random spin
   linearIndex = randi(numel(spin));
   [row, col]  = ind2sub(size(spin), linearIndex);
   % Find nearest neighbors
   above = mod(row - 1 - 1, size(spin,1)) + 1;
   below = mod(row + 1 - 1, size(spin,1)) + 1;
   left  = mod(col - 1 - 1, size(spin,2)) + 1;
   right = mod(col + 1 - 1, size(spin,2)) + 1;
   neighbors = [spin(above,col);spin(row,left);spin(row,right);spin(below,col)];
   % Calculate energy change if this spin is flipped
   dE = 2 * J * spin(row, col) * sum(neighbors);
   % Boltzmann probability of flipping
   prob = exp(-dE / kT);
   % Spin flip condition
   if dE <= 0 || rand() <= prob spin(row, col) = - spin(row, col);end
end
```

APPENDIX 2 – KTB MAIN WELL CORE POROPERM DATA

[http://www-icdp.icdp-online.org/sites/ktb/welcome.html]

Depth (m)	κ(μD)	φ (%)	Orient #	Sample	Batch	Orient Letter
4151.73	7.35	.712	0	%H001D33P1	%HB1	s=perpend
4151.73	51.9	.726	1	%H001D33P2	%HB1	p=parallel
4153.61	3.5	.361	2	%H001G54P1	%HB1	a=axial
4153.61	3.8	.276	2	%H001G54P2	%HB1	a
4251.37	14.8	.509	1	%H003A5P2	%HB1	p
4251.40	4.2	.516	0	%H003A5P1	%HB1	s
4341.70	1.06	.477	0	%H004A4aP1	%HB1	s
4341.70	1.6	.512	1	%H004A4aP2	%HB1	p
4449.57	64	.914	3	%H005D32P1	%HB1	r=radial
4449.57	16.3	.836	2	%H005D32P2	%HB1	a
4513.80	11.4	.548	0	%H006C18bP1	%HB1	s
4513.92	3	.242	1	%H006C18bP2	%HB1	p
4593.22	241	.565	1	%H007B7aP2	%HB1	p
4593.25	1.66	.393	0	%H007B7aP1	%HB1	s
4648.10	2.9	.406	1	%H008C33P1	%HB1	p
4648.10	11.6	.621	3	%H008C33P2	%HB1	r
4688.71	2.3	.399	3	%H009F40P1	%HB1	r
4688.71	2.9	.511	2	%H009F40P2	%HB1	a
4820.84	77.1	2.23	3	%H010B10P1	%HB1	
4820.84	9.4	1.32	2	%H010B10P2	%HB1	a
5012.25	3	.539	2	%H011A5aP1	%HB1	a
5012.25	5.6	.652	3	%H011A5aP2	%HB1	r
5083.35	10.1	.606	3	%H012B29aP1	%HB1	r
5083.35	37.6	.764	3	%H012B29aP2	%HB1	r
5282.00	65.7	.691	0	%H013A1P1	%HB1	s
5282.00	62.8	.701	1	%H013A1P2	%HB1	p
5382.19	1.72	.344	3	%H014G38aP1	%HB1	r
5382.19	0.51	.34	2	%H014G38aP2	%HB1	a
5382.19	0.635	.303	2	%H014G38aP3	%HB1	a

```
%6150.05          0.136  .907      1        %H023D20aP1  %HB1a     p
6150.06  4.54    .615     3        %H023D20aP2  %HB1a     r
6150.06  4.28    .692     0        %H023D20aP3  %HB1a     s
```